Journal Pre-proof

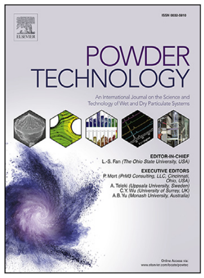

Understanding ice crystal melting in an icing wind tunnel through two-way coupled CFD simulation

Xin Yang, Chuxiao Zhang, Xu Wang, Joel Guerrero, Jan Oscar Pralits, Xuerui Mao

PII: S0032-5910(26)00584-X
DOI: https://doi.org/10.1016/j.powtec.2026.122695
Reference: PTEC 122695

To appear in: *Powder Technology*

Received date : 4 January 2026
Revised date : 3 April 2026
Accepted date : 16 May 2026

Please cite this article as: X. Yang, C. Zhang, X. Wang et al., Understanding ice crystal melting in an icing wind tunnel through two-way coupled CFD simulation, *Powder Technology* (2026), doi: https://doi.org/10.1016/j.powtec.2026.122695.

Graphical Abstract

Understanding ice crystal melting in an icing wind tunnel through two-way coupled CFD simulation

Xin Yang, Chuxiao Zhang, Xu Wang, Joel Guerrero, Jan Oscar Pralits, Xuerui Mao

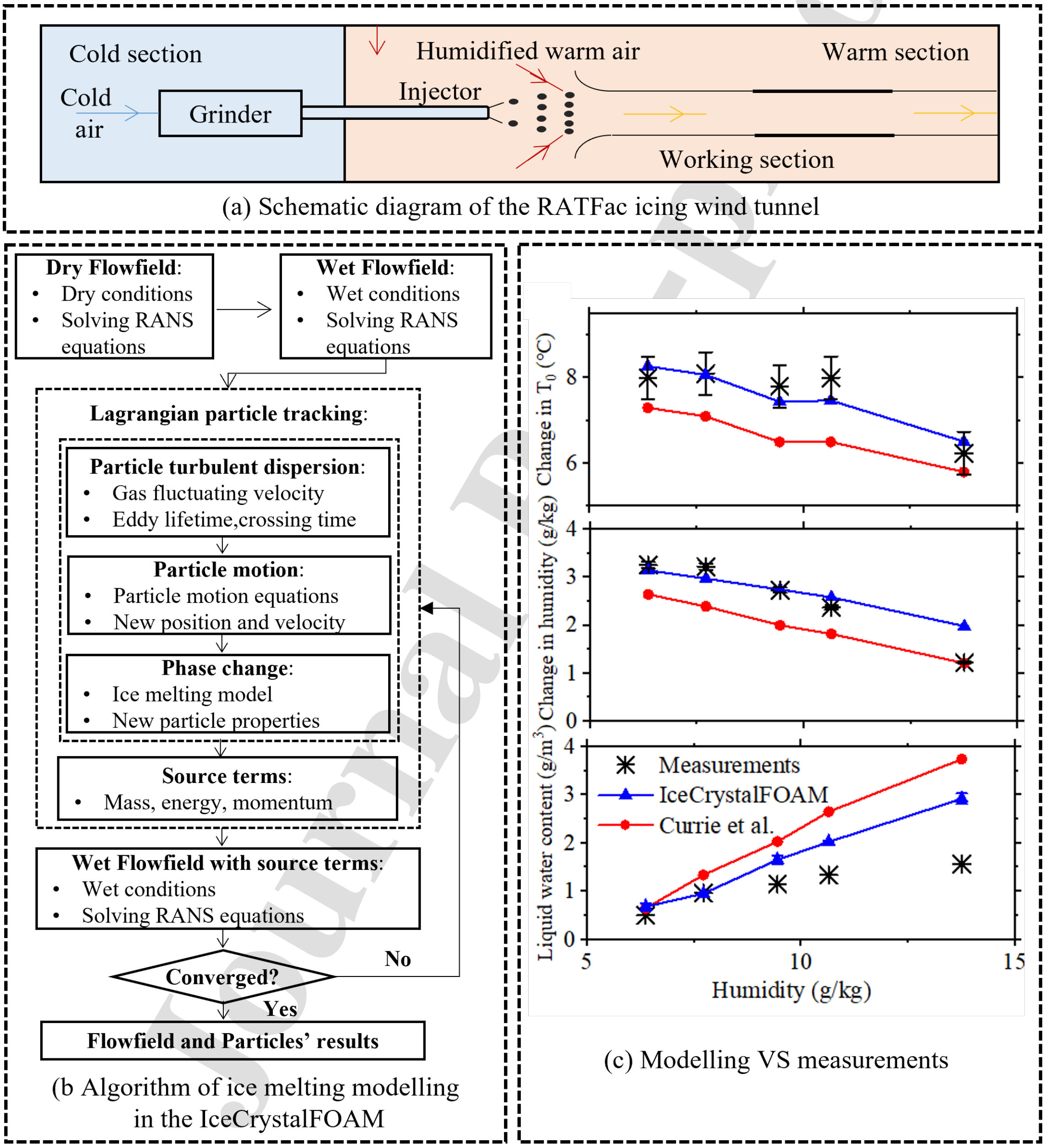

Highlights

Understanding ice crystal melting in an icing wind tunnel through two-way coupled CFD simulation

Xin Yang, Chuxiao Zhang, Xu Wang, Joel Guerrero, Jan Oscar Pralits, Xuerui Mao

- A new two-way coupled CFD solver for ice-crystal melting is developed.
- The solver is validated through code-to-code comparison and experimental data.
- Parametric studies of flow and particle conditions yield consistent results.
- Numerical uncertainties related to particle injection properties are assessed.

Understanding ice crystal melting in an icing wind tunnel through two-way coupled CFD simulation

Xin Yang[a,b,*], Chuxiao Zhang[a], Xu Wang[a], Joel Guerrero[c], Jan Oscar Pralits[d], Xuerui Mao[a,e]

[a] *State Key Laboratory of Explosion Science and Safety Protection, Beijing Institute of Technology, Beijing, China*
[b] *Yangtze Delta Region Academy, Beijing Institute of Technology, Jiaxing, China*
[c] *Wolf Dynamics SRL, Genova, Italy*
[d] *DICCA, University of Genoa, Genova, Italy*
[e] *Beijing Institute of Technology (Zhuhai), Beijing, China*

Abstract

Ice crystal icing poses a significant threat to aircraft engine safety. The sticking potential of ice crystals is mainly determined by ice melting behavior, but the coupled behavior of ice melting, turbulent dispersion, and the gas flow remains insufficiently understood. This study develops a new two-way coupled Eulerian–Lagrangian solver integrated into OpenFOAM to simulate the transport and melting behavior of ice crystals. The three-stage phase-change model is employed to capture particle melting, while turbulent dispersion is represented using the discrete random walk model. A parametric study is conducted to investigate the effects of flow conditions and particle properties on melting behavior in an icing wind tunnel. The solver is validated through code-to-code comparison and experimental data. The predicted variations in gas temperature and humidity due to two-way coupling align well with measurements, whereas the liquid water content is qualitatively consistent but overestimated. Increasing humidity, total temperature, pressure, and particle aspect ratio enhances melting potential, while higher Mach numbers and larger particle sizes reduce it. The influence of uncertainties in particle injection boundary conditions reported in the literature is also discussed.

Keywords: Particle melting, CFD, Multiphase flow, Eulerian–Lagrangian model, Ice crystal, Icing wind tunnel

1. Introduction

Ice crystal icing (ICI) in jet engines can lead to engine surge, stall, flameout and even compressor damages due to ice shedding [1, 2]. To mitigate the threat, the FAA and EASA have introduced new

*Corresponding author
Email address: xinyang.ruijin@bit.edu.cn, tel: +86 17610956070 (Xin Yang)

engine certification requirements, including Amendment 34 of 14 CFR 33 and Amendment 4 of CS-E and Amendment 16 of CS-25, which define the icing envelope and the characteristics of ice crystals (specifically a median mass size range from 50 to 200 μm and a total water content between 1 and 5 g/m^3). Over the past decades, NRC (National Research Council), NASA (National Aeronautics and Space Administration), Technische Universität Braunschweig and Cox have conducted extensive icing wind tunnel tests to investigate icing physics, including particle transport [3, 4, 5], phase change [3, 5, 6], sticking/erosion/fragmentation [7, 8, 9, 10], thermodynamic interactions with heated walls [11, 12, 13], and engine-representative rigs [14, 15]. These studies have demonstrated a plateau in icing severity for melt ratios between 10%-23% by Currie et al. [7] and 9%-13% by Bucknell et al. [8], highlighting the critical role of melt ratio in influencing particle sticking, erosion, and thermodynamic behavior. Therefore, a detailed understanding and accurate prediction of ice crystal melting behavior in icing wind tunnels is essential for reliable ICI prediction.

Ice crystal melting in icing wind tunnels is a typical dilute [1], particle-laden flow with phase change. A spectrum of computational fluid dynamics (CFD) approaches exists for particle-laden flows [17, 18, 19, 20], including particle-resolved direct numerical simulation (PR-DNS), point-particle DNS (PP-DNS), point-particle large-eddy simulation (PP-LES), and point-particle Reynolds-averaged Navier–Stokes (PP-RANS). In PR-DNS, the flow around each particle is fully resolved, and particle kinematics evolve under resolved fluid forces; this approach is mainly used to study micro-scale particle–fluid interactions and to develop the correlations for aerodynamic coefficients (drag force coefficient, lift force coefficient, etc.) needed in the point-particle methods. In PP-DNS, particles are modeled as point sources of momentum, mass, and energy, valid when the particle diameter is smaller than the Kolmogorov length scale. Sub-models (drag, lift, etc.) are needed to estimate the forces acting on the particle. PP-LES advances the particle equations of motion on a filtered flow field obtained from the LES of the Navier–Stokes equations; because LES permits coarser grids than DNS, larger particles are tractable, but subgrid contributions to the fluid velocity at the particle location must be modeled when they significantly affect particle motion [17, 19]. Despite their fidelity, DNS/LES-based methods remain computationally expensive for engineering studies. In contrast, PP-RANS is widely used in real applications. The method requires additional turbulence model to close the RANS equations, aerodynamic coefficient models to calculate the fluid

[1]For a typical RATFac (Research Altitude Test Facility) icing wind tunnel condition with the total ice content = 8 g/m^3, the particle volume fraction is approximately 8.7×10^{-6}, well below Elghobashi's dilute particle-laden flow threshold of 5×10^{-4} [16].

forces on particle [21], and particle turbulent dispersion model to calculate the fluctuating fluid velocity [22]. Within PP-RANS, the particle phase can be treated by an Euler–Euler (interacting continua) or an Euler–Lagrange (dispersed, discrete particles) formulation. The Euler-Lagrange approach has the advantage to consider the discrete nature of the dispersed particle phase, in which multiple physical effects (particle size distribution, particle-turbulence interaction, particle-wall interaction, etc.) can be modelled on the basis of the first physical principles [18]. Therefore, the Euler-Lagrange based PP-RANS method is adopted for the prediction and understanding of ice crystal melting behaviour in the RATFac icing wind tunnel.

Euler–Lagrange PP-RANS solvers with phase change have been developed for drying, combustion, and related processes, typically using the lumped-capacitance assumption (particle temperature uniform in space, varying in time) [23, 22, 24, 25]. Evaporation/condensation is modeled by adding heat and mass transfer terms to the particle energy and mass balance equations and to the two-way source terms in the carrier phase [26]; such capabilities are available in the well-known commercial CFD solver ANSYS Fluent [27] and in the open-source CFD solver OpenFOAM [28]. However, most of these existing solvers only consider the evaporation/condensation processes in the phase change model while the melting process due to the latent heat transfer is not considered yet. For ice crystals, the lumped-capacitance assumption is justified under typical icing conditions because the Biot number (the ratio of the thermal resistance for conduction inside a solid to the resistance for convection at its surface) is below the 0.1 threshold [29, 30], enabling a compact phase-change model with three states: fully solid, partially melted, and fully melted. Several studies have developed a similar detailed phase change model for ice crystal melting based on the experiments of the melting behaviour of a single ice crystal in an acoustic levitator and the relative difference between predicted and measured melting times is approximately 15% to 25% [31, 30, 32, 33], supporting the method's validity for predicting ice crystal melting behavior. However, the melting behavior of ice crystals in real icing wind tunnels and jet engines is influenced not only by the phase change of the particles themselves but also by their transport and interactions with the gas phase.

Currie et al. [3] conducted the first modeling of the two-way coupled melting behavior of ice crystals in the RATFac icing wind tunnel. Several simplifications were made, including: 1) The use of an empirical nonsphericity correction factor, derived from the melting behavior of nonspherical ice crystal particles in the acoustic levitator, to account for the nonspherical geometry; and 2) Ice particles were placed near the injection pipe walls, based on the visual observation that particles were concentrated near the pipe walls. Additionally, particle turbulent dispersion was considered using the discrete random walk model. This was because particles were injected through a single injection pipe, and the turbulent dispersion played a significant role in creating a relatively uniform distribution in the working section. Currie et al. [3] observed that the model reasonably predicted the changes in air temperature and humidity due to particle evaporation and melting. However, the predicted liquid water content was more than double the measured values in the higher melt ratio range. The authors suggested that the measurements may have been under-evaluated. Recently, Parker et al. [5] numerically investigated the melting behavior of ice crystals in the same wind tunnel using methods similar to those of Currie et al. [3]. The key differences between their model and Currie et al.'s approach are: (i) the treatment of nonsphericity in phase change, which directly uses the aspect ratio of ice particles in the phase change model, rather than using the empirical correction factor that may overestimate the impact of nonsphericity on ice melting, and (ii) particles are uniformly spaced at the inlet, rather than being concentrated near the wall. Good agreement was found between the predicted and measured melt ratios for medium to low melt ratios (approximately 5% to 10%) similar to those of Currie et al. [3] while the higher melt ratio range was not presented in the study. In addition to the melting behavior in the RATFac facility, Soubrié et al. [34] modeled particle transport, fragmentation, and melting in the ICE-MACR (Ice Crystal Environment - Modular Axial Compressor Rig) installed at the AIWT (Altitude Icing Wind Tunnel) icing wind tunnel, though two-way interphase coupling was not considered. It was observed that the predicted melt ratio was much smaller than the measurements, especially at lower melt ratios. Furthermore, several other studies have modeled the melting behavior of ice crystal particles in compressors without experimental validation. These studies aim to enable rapid evaluation of melting in engines using one dimensional methods [35, 29], to compare the performance and differences between Eulerian and Lagrangian approaches [36], and to investigate detailed melting behavior in engine-representative geometries [37, 32, 38].

Overall, numerical studies on ice crystal melting have advanced modeling capabilities and enhanced understanding of melting physics. However, only a limited number of studies have compared melting behavior in wind tunnels and at engine-representative conditions against experimental measurements, and discrepancies in modeling settings and performance still exist. Detailed understanding of the coupled behavior among ice phase change, turbulent dispersion, and gas flow remains limited. Therefore, this study aims to: (1) develop a two-way coupled Eulerian–Lagrangian ice melting solver that accounts for both nonspherical ice phase change and particle turbulent dispersion; and (2) improve understanding of the coupled behavior among ice phase change, turbulent dispersion, and gas flow. The modeling of ice crystal melting is conducted using the 3D CFD code IceCrystalFOAM. Simulation results are compared with experimental data on gas temperature, humidity, and liquid water content to evaluate the model's performance.

2. Mathematical models

IceCrystalFOAM is a two-way coupled Euler–Lagrange particle-laden flow solver, developed on the OpenFOAM framework [28] to predict ice-crystal melting in the RATFac icing wind tunnel. This method solves the governing equations for fluid–particle two-phase flow, comprising a continuous phase module that resolves the Reynolds-averaged Navier–Stokes (RANS) equations for the fluid, and a discrete phase module that tracks particles by solving Newton's laws of motion.

2.1. Continuous phase

The continuous phase module computes the flow fields—including gas velocity, temperature, pressure, composition, and turbulence—which are essential for particle tracking and phase change modeling. To reduce computational cost, a steady-state assumption is commonly employed in the continuous phase modeling of existing icing codes[39, 36, 40, 41] for icing wind tunnel conditions, whereas transient simulations are often used to capture the unsteady flow in real engines [38, 42]. Consequently, the governing equations of the continuous phase is expressed as the steady multi-species compressible Reynolds-averaged Navier–Stokes (RANS) equations, as follows:

$$
\begin{cases}
\nabla \cdot (\rho \overline{\boldsymbol{U}}) = S_{mass} \\
\nabla \cdot [\rho \overline{\boldsymbol{U}} \otimes \overline{\boldsymbol{U}}] = -\nabla \overline{p} + \nabla \cdot [\overline{\boldsymbol{\sigma}} - \rho \overline{\boldsymbol{U'U'}}] + S_{mom} \\
\nabla \cdot [\rho \overline{\boldsymbol{U}} \overline{e}] = -\nabla [\overline{p} \overline{\boldsymbol{U}}] + \nabla \cdot (\overline{\boldsymbol{\sigma}} \cdot \overline{\boldsymbol{U}}) + \nabla \cdot (\lambda_{\text{eff}} \nabla \overline{T}) - \nabla \cdot (\overline{h \boldsymbol{J}}) + S_{energy} \\
\nabla \cdot (\rho \overline{\boldsymbol{U}} \overline{Y}) = -\nabla \cdot \overline{\boldsymbol{J}} + S_{species}
\end{cases}
\tag{1}
$$

where, ρ is gas density; $\overline{\boldsymbol{U}}$, $\overline{p}$, $\overline{e}$, $\overline{T}$, $\overline{Y}$, $\overline{h}$, and $\overline{\boldsymbol{J}}$ are Reynolds-averaged gas velocity, pressure, specific energy (the sum of internal and kinetic energies per unit mass), temperature, species mass fraction, specific enthalpy of species, and diffusion flux of species ($=(\rho D_{\text{eff}} \nabla \overline{Y})$), respectively. The gas phase is modelled as a three-species humid-air mixture consisting of water vapour, oxygen, and nitrogen. The mixture is assumed to obey the ideal-gas equation of state. $\overline{\boldsymbol{\sigma}}$ is Reynolds-averaged viscous stress tensor, which is the sum of a shear stress term proportional to the symmetric velocity gradient and an isotropic viscous stress term proportional to the velocity divergence. λ_{eff} is effective gas thermal conductivity, which is the sum of molecular and turbulent thermal conductivity; D_{eff}

is the total mass diffusivity, which is the sum of molecular and turbulent mass diffusivity. Based on the unity Lewis number assumption, the turbulent mass diffusivity is equal to the turbulent thermal diffusivity. S_{mass}, S_{mom}, S_{energy}, and $S_{species}$ are the source terms of mass, moment, energy and species transferred from the discrete phase to the continuous phase. The term $\rho\overline{\boldsymbol{U'U'}}$ in Equation 1 is Reynolds stress tensor, which introduces the correlations of fluctuating velocity components and must be modeled to close the RANS equations. In this study, the standard two-equation $k-\epsilon$ turbulence model is adopted to model the effects of turbulence [3, 43, 44]. The model introduces two additional transport equations for the turbulent kinetic energy k and the turbulence dissipation rate ϵ, enabling the computation of the eddy viscosity and closure of the RANS system. The SIMPLEC (SIMPLE consistent) algorithm [45] is employed to resolve the pressure-velocity coupling, and second-order discretization schemes are used to discretize the gradient, divergence, and Laplacian terms of the RANS equations.

2.2. Discrete phase

The discrete phase module computes particle transport and phase change behavior. For particle transport, it incorporates the governing equations for particle motion and turbulent dispersion, as well as the introduction of particle-wall interaction. For phase change, it includes the lumped-capacity-based ice melting model and two-way fluid-particle coupling methods.

2.2.1. Particle transport

The translational motion of the discrete phase is governed by force balance equations:

$$\begin{cases} \dfrac{\mathrm{d}\boldsymbol{X}_\mathbf{p}}{\mathrm{d}t} = \boldsymbol{U}_\mathbf{p} \\ m_\mathrm{p}\dfrac{\mathrm{d}\boldsymbol{U}_\mathbf{p}}{\mathrm{d}t} = \boldsymbol{F}_{\mathbf{D},\boldsymbol{p}} + \boldsymbol{F}_\mathbf{p} \\ \boldsymbol{F}_{\mathbf{D},\boldsymbol{p}} = \dfrac{1}{8}\rho C_\mathrm{D}\pi D_\mathrm{p}^2 \left|\boldsymbol{U} - \boldsymbol{U}_\mathbf{p}\right| (\boldsymbol{U} - \boldsymbol{U}_\mathbf{p}) \end{cases} \tag{2}$$

where, $\boldsymbol{U}$ is gas velocity; $\boldsymbol{X}_\mathbf{p}$, $\boldsymbol{U}_\mathbf{p}$, m_p and D_p are particle location, particle velocity, particle mass and particle diameter, respectively; $\boldsymbol{F}_{\mathbf{D},\boldsymbol{p}}$ is the drag force, which acts in the opposite direction of the relative motion of particles with respect to the fluid flow; $\boldsymbol{F}_\mathbf{p}$ are other forces, including lift forces, gravity, virtual mass force, etc., which are neglected in this study due to the high inertia of the ice crystals. C_D is the drag coefficient. The correlations of C_D proposed by Haider and Levenspiel [46], which is as a function of particle Reynolds number ($\mathrm{Re}_\mathrm{p} = \rho\left|\boldsymbol{U} - \boldsymbol{U}_\mathbf{p}\right| D_\mathrm{p}/\mu$ and μ is gas viscosity) and shape factor (ϕ, the ratio of the surface area of a sphere having the same volume as the particle to the actual surface area of the particle), are used in this study. In order to balance the computational accuracy and time, the motion equations are integrated via the analytic discretization method [47].

The dispersion of ice crystals due to turbulence in the continuous phase plays a critical role in determining particle transport and phase change behavior in the mixing region and working section of the RATFac icing wind tunnel, where measured turbulence intensities range from 7.7% to 10.4% for Mach numbers between 0.25 and 0.4. Turbulent dispersion is modeled using the Discrete Random Walk Model (DRWM) [48, 49], which integrates the particle motion equation based on the instantaneous gas velocity ($\boldsymbol{U} = \overline{\boldsymbol{U}} + \boldsymbol{U'}$) presented in Equation (2). The DRWM is accomplished based on two key assumptions [48, 49]: i) particles interact with a sequence of turbulent eddies, and the interaction time—governing how often the fluctuating velocity is re-randomly sampled—is the lesser of the eddy lifetime, t_e and eddy crossing time, t_{cross}; ii) the fluctuating velocity ($\boldsymbol{U'}$) within each eddy follows a Gaussian distribution with a standard deviation of $\boldsymbol{U'_{std}} = \sqrt{2k/3}$. Thus, the DRWM is mathematically described as follows:

$$\begin{cases} \boldsymbol{U'} = \zeta\sqrt{2k/3} \\ t_e = 2C_{\mathrm{TS}}\dfrac{k}{\epsilon} \\ t_{cross} = -\dfrac{\rho_p D_p^2}{18\mu} ln\left[1 - \left(\dfrac{18\mu}{\rho_p D_p^2}\dfrac{L_{\mathrm{e}}}{|\boldsymbol{U} - \boldsymbol{U}_{\mathbf{p}}|}\right)\right] \end{cases} \tag{3}$$

where, ζ is a normally distributed random number; C_{TS} is the time scale constant; ρ_p is particle density; L_{e} is the eddy length scale. To ensure sufficient particle sampling for turbulent dispersion analysis, 100 particles are released from each injection point [3].

Particle-wall interaction governs the rebound behavior of impinging particles. In this study, the method proposed by Trontin et al. [50] is adopted, which classifies the rebound behavior into three regimes based on a dimensionless parameter, representing the ratio of the normal kinetic energy to the surface energy.

2.2.2. Particle phase change

Ice melting behavior is governed by the heat and mass transfer of ice crystal particles. Due to the low Biot number in typical icing conditions, the lumped capacitance method is commonly used to model the phase change of ice crystals, assuming a spatially uniform particle temperature that varies over time. The phase change process is assumed to consist of three stages: (1) the fully solid ice crystal stage with an unchanged particle shape, (2) the partially melted ice crystal stage with increasing sphericity as the melt ratio increases, reaching unity at complete melting, and (3) the fully melted stage with a spherical shape. The sphericity-dependent heat and mass transfer correlations proposed by Villedieu et al. [50] are used to account for its effect on particle melting behavior. Additionally, ice particles undergo surface blowing, modeled by the method proposed by Renksizbulut and Yuen [51], where the Nusselt and Sherwood numbers are multiplied by the surface blowing factor—dependent on the particle's thermal properties and the slip temperature between the particle and gas phases. Based on these assumptions, the governing equations of the phase change model are as follows:

Stage 1: fully solid ice crystals

$$\begin{cases} m_\mathrm{p} c_\mathrm{p,i} \dfrac{\mathrm{d}T_\mathrm{p}}{\mathrm{d}t} = Q_{\mathrm{conv},p} - \dot{m}_{\mathrm{sub},p} L_\mathrm{s} \\ \dfrac{\mathrm{d}m_\mathrm{p}}{\mathrm{d}t} = -\dot{m}_{\mathrm{sub},p} \\ Q_{\mathrm{conv},p} = \dfrac{\pi D_\mathrm{p}}{\Phi} \mathrm{Nu}^* \lambda (T_\mathrm{f} - T_\mathrm{p}) \\ \dot{m}_{\mathrm{sub},p} = \dfrac{\pi D_\mathrm{p}}{\Phi} \mathrm{Sh}^* \rho D_\mathrm{v,g} (\gamma_\mathrm{v,p} - \gamma_\mathrm{v,g}) \end{cases} \tag{4}$$

where, $c_\mathrm{p,i}$ is the specific heat of ice, L_s is the total latent heat of fusion (L_f) and evaporation (L_v), Φ is the particle sphericity; Nu^* and Sh^* are the Nusselt number and Sherwood number multiplied by the surface blowing factor using the correlations proposed by Villedieu et al. [50] and Renksizbulut and Yuen [51]; T_f is the gas temperature local to the particle; $D_\mathrm{v,g}$ is the water vapour diffusivity in the air, $\gamma_\mathrm{v,p}$ and $\gamma_\mathrm{v,g}$ are the vapour mass fraction at the particle surface and gas phase, respectively.

Stage 2: start of ice melting → 100% liquid

$$\begin{cases} Q_{\mathrm{conv},p} = \dot{m}_{\mathrm{evap},p} L_\mathrm{v} + \dot{m}_{\mathrm{melt},p} L_\mathrm{f} \\ \dfrac{\mathrm{d}m_\mathrm{p}}{\mathrm{d}t} = -\dot{m}_{\mathrm{evap},p} \\ \dfrac{\mathrm{d}m_\mathrm{p,i}}{\mathrm{d}t} = -\dot{m}_{\mathrm{melt},p} \\ Q_{\mathrm{conv},p} = \dfrac{\pi D_\mathrm{p}}{\Phi} \mathrm{Nu}^* k_\mathrm{g} (T_\mathrm{f} - T_\mathrm{p}) \\ m_\mathrm{p,w} = m_\mathrm{p} - m_\mathrm{p,i} \\ \dot{m}_{\mathrm{evap},p} = \dfrac{\pi D_\mathrm{p}}{\Phi} \mathrm{Sh}^* \rho D_\mathrm{v,g} (\gamma_\mathrm{v,p} - \gamma_\mathrm{v,g}) \\ \mathrm{MR}_\mathrm{p} = \dfrac{m_\mathrm{p,w}}{m_\mathrm{p}} \end{cases} \tag{5}$$

where, the subscripts i and w represent ice and water, $\dot{m}_\mathrm{melt}$ is the melting mass flux determined by the heat transfer equation of Equations (5). MR_p is the particle melt ratio. The melt ratio of the flowfield, MR_f, is mapped from the particle melt ratio to the field and defined by the ratio of liquid water content (LWC) to total water content (TWC).

$$\begin{cases} \mathrm{TWC} = \dfrac{\sum (n_p m_\mathrm{p} \Delta t_\mathrm{p})}{\Delta t_\mathrm{f} V} \\ \mathrm{LWC} = \dfrac{\sum (n_p m_\mathrm{p} \mathrm{MR_p} \Delta t_\mathrm{p})}{\Delta t_\mathrm{f} V} \\ \mathrm{MR_f} = \dfrac{\mathrm{LWC}}{\mathrm{TWC}} \end{cases} \tag{6}$$

where, n_p represents the particle count per parcel, Δt_p is the particle time step, Δt_f is the flow time step (1 s for steady flow in OpenFOAM), the symbol $\sum$ denotes the summation of particle quantities passing through a control volume, and V is the cell volume.

Stage 3: fully melted, 100% liquid

$$\begin{cases} m_\mathrm{p} c_\mathrm{p,w} \dfrac{\mathrm{d}T_\mathrm{p}}{\mathrm{d}t} = Q_{\mathrm{conv},p} - \dot{m}_{\mathrm{evap},p} L_\mathrm{v} \\ \dfrac{\mathrm{d}m_\mathrm{p}}{\mathrm{d}t} = -\dot{m}_{\mathrm{evap},p} \\ Q_{\mathrm{conv},p} = \dfrac{\pi D_\mathrm{p}}{\Phi} \mathrm{Nu}^* k_\mathrm{g} (T_\mathrm{f} - T_\mathrm{p}) \\ \dot{m}_{\mathrm{evap},p} = \dfrac{\pi D_\mathrm{p}}{\Phi} \mathrm{Sh}^* \rho D_\mathrm{v,g} (\gamma_\mathrm{v,p} - \gamma_\mathrm{v,g}) \end{cases} \tag{7}$$

2.2.3. Two-way coupling

Two-way coupling involves the exchange of mass, energy, and momentum between the phases, allowing the discrete phase to influence the continuous phase. Ice crystal icing tests conducted in the RATFac wind tunnel showed a noticeable decrease in tunnel temperature and an increase in humidity following the injection of ice crystal particles. The transfer of mass, energy, and momentum from the discrete phase to the continuous phase is computed by summing the changes in these quantities as particles pass through each control volume. In the two-way coupling, mass transfer results from the sublimation and evaporation of water species; energy transfer primarily arises from changes in thermal and phase change energy, mathematically equivalent to the convective heat transfer term (Q_conv) in the energy equation of the phase change model; and momentum transfer is driven by the drag force. Consequently, the source terms for two-way coupling are expressed as follows:

$$\begin{cases} \displaystyle\int_V S_{mass} dV = \sum_p (n_p (\dot{m}_{\mathrm{sub},p} + \dot{m}_{\mathrm{evap},p})) \\ \displaystyle\int_V S_{energy} dV = -\sum_p (n_p Q_{\mathrm{conv},p}) \\ \displaystyle\int_V S_{mom} dV = -\sum_p (n_p F_{\mathrm{D},p} \Delta t_\mathrm{p}) \end{cases} \tag{8}$$

where, $\int_V S_{mass}dV$, $\int_V S_{energy}dV$, and $\int_V S_{mom}dV$ are the volume integrals of each source term; the subscript p represents the particle index of particles located in the considered computational cell (control volume). The volume integral of the species source term is mathematically equivalent to that of the mass source term as water vapor is the only species undergoing phase change. As shown in Fig. 1, the two-way coupling procedure involves: (1) solving the RANS equations to obtain the dry flowfield without particle tracking until convergence and determining the total temperature and humidity at the plenum inlet, (2) switching to the wet condition and solving the RANS equations without particle tracking until convergence, (3) performing particle tracking by solving particle transport, phase change, and source terms of two-way coupling for RANS equations, (4) solving the RANS equations with the source terms from the previous step at the specified discrete phase interval, and (5) iterating steps 3 and 4 until convergence. More details of the computational settings can be found in section 3.2 Numerical set-up.

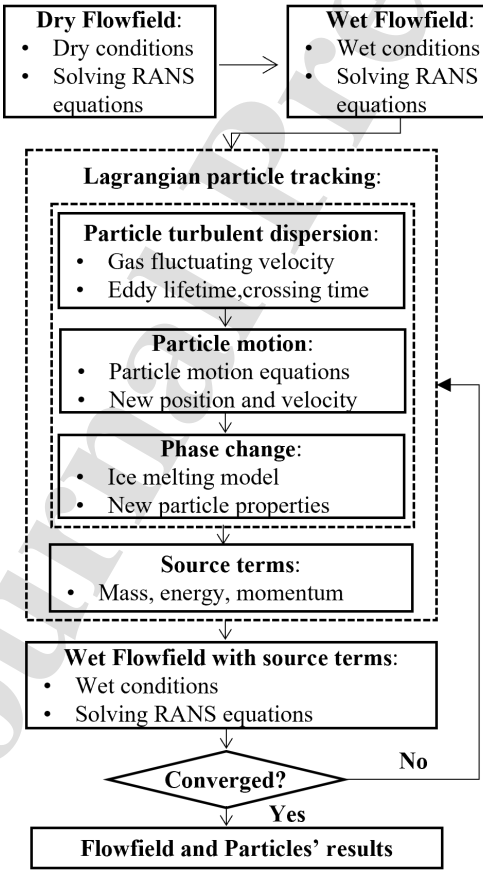

Figure 1: Algorithm of ice crystal melting modelling in the IceCrystalFOAM.

3. Case description and setup

3.1. Case description

Ice crystal melting experiments were conducted by Currie et al. [3, 52] in the NRC RATFac icing wind tunnel to enhance the understanding of ice crystal melting physics and to provide a database for the development and validation of melting models. The facility features an altitude chamber divided into cold and warm sections, as illustrated in Fig. 2. The wind tunnel is initially operated in the dry condition—without ice particle injection—to establish the required flowfield conditions. It is then switched to the wet condition, introducing ice particles into the flow. These particles are generated in the cold section using a grinder system and injected into the warm section through a pipe (of cross section, 54 × 174.5 mm). The distance from the injection pipe outlet to the tunnel inlet bellmouth is approximately 803 mm. In the warm section, ice particles mix with a flow of controlled temperature and humidity before entering the test section (of cross section, 254 × 132 mm). The distance from the tunnel inlet bellmouth to the instrumentation plane in the working section is approximately 1139 mm. Under dry conditions, total pressure, total temperature, and velocity are measured using a traversable three-hole cobra-style probe with an integrated total temperature sensor. Under wet conditions, total temperature and humidity are measured using a traversable NRC-proprietary "TAT-RH" (Total Temperature and Relative Humidity) probe. The liquid water content is determined using the SEA (Science Engineering Associates) multiwire probe to experimentally determine the melting potential. The particle size distribution (PSD) is measured via a laser shadowgraphy technique developed by NRC. Further details on the experiments, facility, and instrumentation can be found in [3, 7, 53, 52].

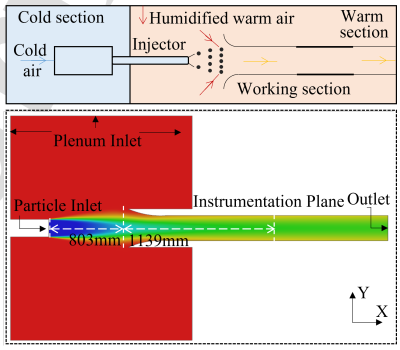

Figure 2: Schematic diagram of the RATFac icing wind tunnel (on the top) and the middle plane of the computational domain with boundary conditions (on the bottom): not to scale.

3.2. Numerical set-up

Ice crystal melting in the wind tunnel is modeled using the Euler–Lagrange approach with two-way coupling, implemented in IceCrystalFOAM. Steady RANS simulations are performed to resolve the aerodynamic flow field. To reduce computational cost, the study focuses on a reduced domain—from the particle injection pipe outlet to the working section—similar to the computational setup used by Currie et al. [3]. As shown in Fig. 2, the computational domain extends from the particle injection pipe discharge and the plenum to an outlet plane. Hexahedral structured meshes with an orthogonal quality larger than 0.6 are generated for the computational domain. More details of the meshes are given in Appendix A. Boundary conditions are set similar to Currie et al. [3], as follows: velocity inlet for the particle inflow, total pressure inlet for the plenum, and static pressure outlet. These pressures are adjusted to match the test section Mach number (Ma) and total pressure. Plenum inlet temperature and humidity are tuned to match the measured centerline total temperature and humidity at the instrumentation plane. Particles are injected 2.5 mm from the injection pipe wall at an ice mass flow rate of 82.3 kg/hr, with initial velocities matching the local flow velocity. The inlet particle size distribution follows a Rosin–Rammler profile with a spread parameter of 1.783, a mean diameter of 61.26 μm, and 25 size intervals, matching measured Dv10, Dv50, and Dv90 values of 23 μm, 45 μm, and 109 μm, respectively [2]. Ice particles are assumed to be prolate spheroids with a uniform aspect ratio of 1.5, consistent with the measured mean aspect ratio [54]. The initial particle temperature is set to −13 $°C$. The turbulence intensity at the inlet is tuned to match the measured centerline turbulence intensity at the instrumentation plane.

To balance computational efficiency with simulation accuracy, a numerical sensitivity study was conducted on both mesh resolution and parcel count for the baseline test case (case 3 in Appendix B). For the mesh sensitivity study, the flowfield parameters—gas velocity, turbulent kinetic energy, gas temperature, and humidity—along the centerline and the upstream and downstream lines of the computational domain [3] were used as evaluation criteria. For the parcel count sensitivity study, the total water content (TWC) at the measurement location and the downstream line served as the primary metric. The grid sensitivity study was performed using four meshes with approximately 0.5M, 1.1M, 2.2M, and 4.4M cells. As shown in Fig. 3, the solution from the 2.2M mesh closely

[2]Dv10, Dv50, and Dv90 represent the particle diameter below 10%, 50% and 90% of the total particle volume is contained, respectively. Dmean is the volume-averaged particle size.

[3]The upstream sampling line is located approximately 0.5 m upstream of the tunnel inlet bellmouth, while the downstream sampling line corresponds to the midline in the y-direction at the measurement plane.

matches that of the 4.4M mesh and the difference is insignificant. Therefore, the mesh is adopted for all subsequent simulations. Figure 4 presents the scaled total water content (with standard deviation) and the averaged standard deviation of the total water content as a function of parcel count from 0.25M to 8M. It is observed that the two parameters gradually converge with the increase
275 in the particle count. The parcel count of 2.0M was selected for the final simulations as the predicted TWC and the mean standard deviation are close to that using 8.0M parcel count.

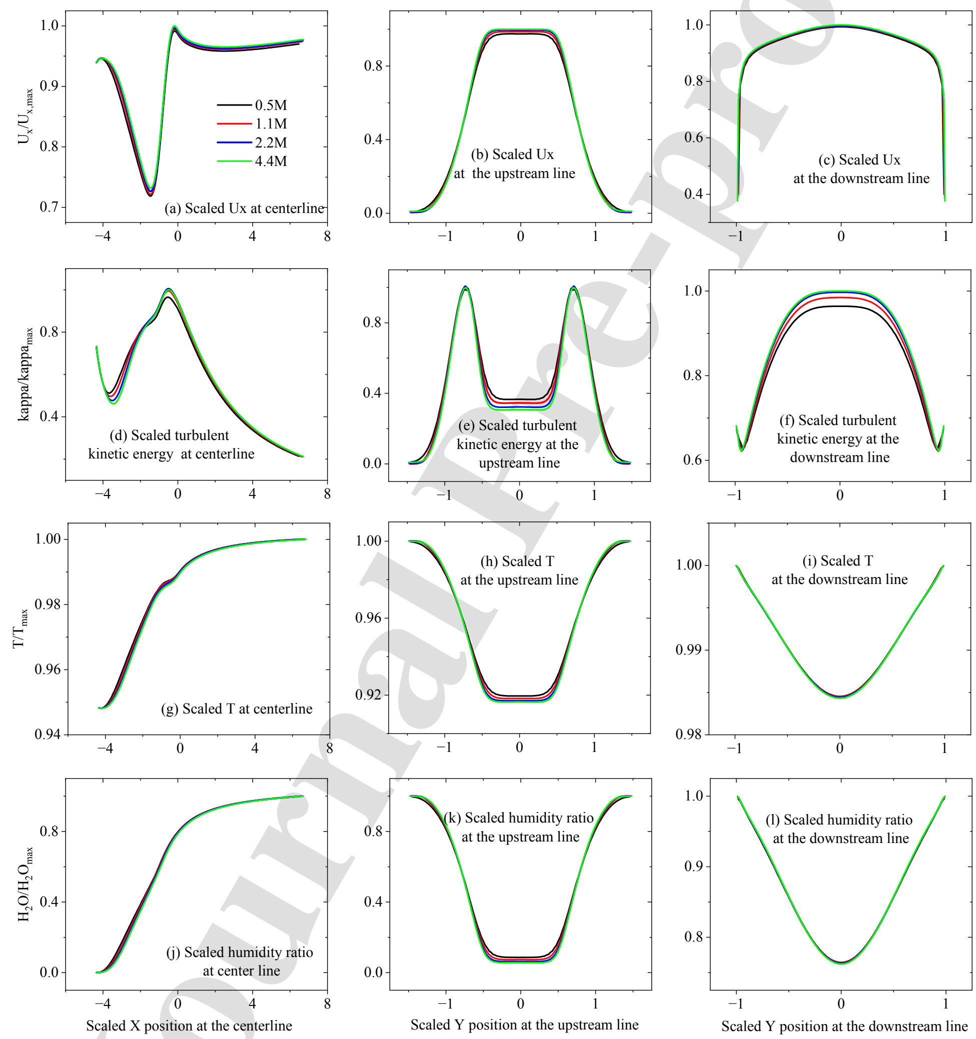

Figure 3: Mesh sensitivity study of the baseline case: (a)–(l) scaled gas velocity at X direction, turbulent kinetic energy, gas temperature and humidity at the centerline and the upstream and downstream lines.

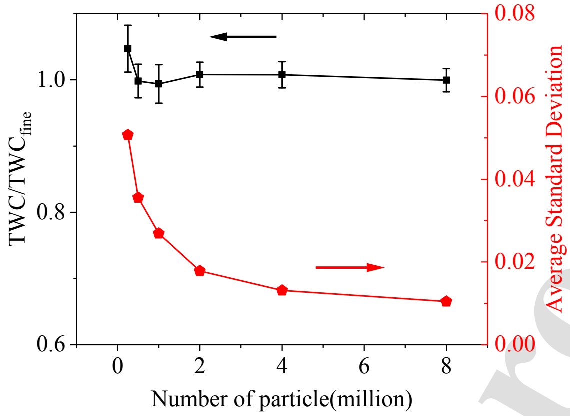

Figure 4: Particle count sensitivity study of the baseline case: the scaled TWC at the measurement location and the mean standard deviation at the downstream line.

4. Results and discussions

4.1. Validation of IceCrystalFOAM

4.1.1. Code-to-code comparison

The ice crystal melting code, IceCrystalFOAM, is compared against both the well-established CFD software ANSYS Fluent and experimental data for the baseline case. For code-to-code comparison, numerical models and settings are closely matched. The standard k-ϵ model is used in both codes to model turbulence in the continuous phase. For the discrete phase, ANSYS Fluent's standard Discrete Phase Model (DPM) is employed without any user-defined functions. To ensure consistency, several adjustments are made in IceCrystalFOAM. First, the ice melting model is disabled, as it is not available in Fluent's DPM. Instead, inert particles are used, with melting physics omitted but heat transfer enabled. Second, the Discrete Random Walk (DRW) model proposed by Gosman et al. [48]—implemented in Fluent—is also adopted in IceCrystalFOAM. This is because the default DRW model in OpenFOAM, which follows a method similar to KIVA codes for estimating eddy lifetime and crossing time [22, 55], tends to overpredict eddy times compared with ANSYS Fluent. Greifzu et al. [56] reported that OpenFOAM's built-in DRW model generally predicts stronger turbulent particle dispersion than ANSYS Fluent. Third, since the particle-wall interaction model by Trontin et al. [50] is not available in ANSYS Fluent, a sticky wall condition is enabled in both codes for comparison.

Accurate flowfield prediction is essential for modeling the melting behavior of ice crystal particles. For example, local gas velocity and turbulent quantities are required to model particle transport—used to compute the drag force in Equation (2) and the fluctuating velocity and eddy times in Equation (3). Meanwhile, gas composition and temperature are needed to model phase change—used to calculate the heat and mass transfer rates in the phase change terms of Equations (4)–(7). Figure 5[4] compares the predicted flowfields from IceCrystalFOAM and ANSYS Fluent. The curves from the two solvers are nearly identical for Ux, turbulent kinetic energy, temperature, and humidity, respectively. In the upstream region, where the central cold injection mixes with the surrounding warm plenum flow, two peaks appear in the turbulent kinetic energy profiles near the injection pipe wall in the y-direction. These peaks result from the interaction between the high-speed injection jet (nearly 70 m/s at the inlet) and the low-speed plenum flow (<2 m/s in most regions). The Ux profile exhibits a flat plateau at the center that decreases toward the plenum, while the temperature and humidity profiles show opposite trends. These features are consistent with the operating conditions of the injection and plenum flows. Further downstream into the working section, all profiles gradually flatten.

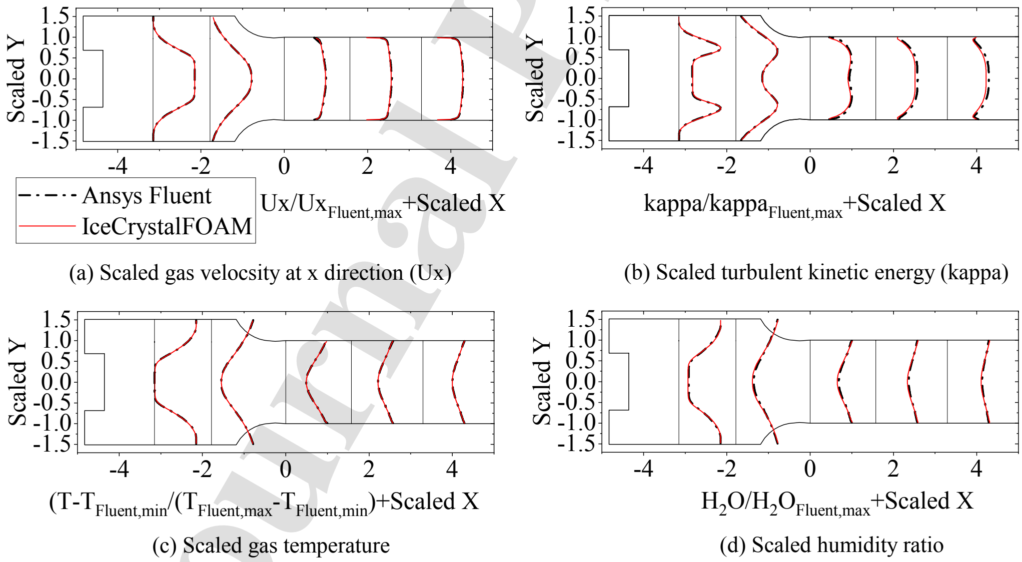

Figure 5: Comparison of the scaled flowfields from simulations in IceCrystalFOAM and ANSYS Fluent:(a) gas velocity at x direction, (b) turbulent kinetic energy, (c) gas temperature, and (d) humidity.

[4]Humidity in the plots is expressed as the humidity ratio (g H_2O per kg dry air); this definition is used in all figures.

Figure 6(a)-(c) show the predicted single-particle tracking results with the particle size of Dv50 from IceCrystalFOAM and ANSYS Fluent without the DRW model enabled. The profiles of scaled particle position, particle Ux, and particle temperature closely overlap between the two solvers. Figure 6(d) also presents the predicted total water content (TWC) of Rosin–Rammler distributed particles from both solvers with the DRW model enabled, again showing close agreement. Particles are released 2.5 mm from the injection pipe wall, following Currie et al. [3]. In the upstream region, this leads to two narrow peaks in the TWC profiles along the y-direction near the pipe wall. With increasing downstream distance, particle turbulent dispersion causes these peaks to gradually vanish, resulting in relatively uniform profiles, particularly in the central region of the test section.

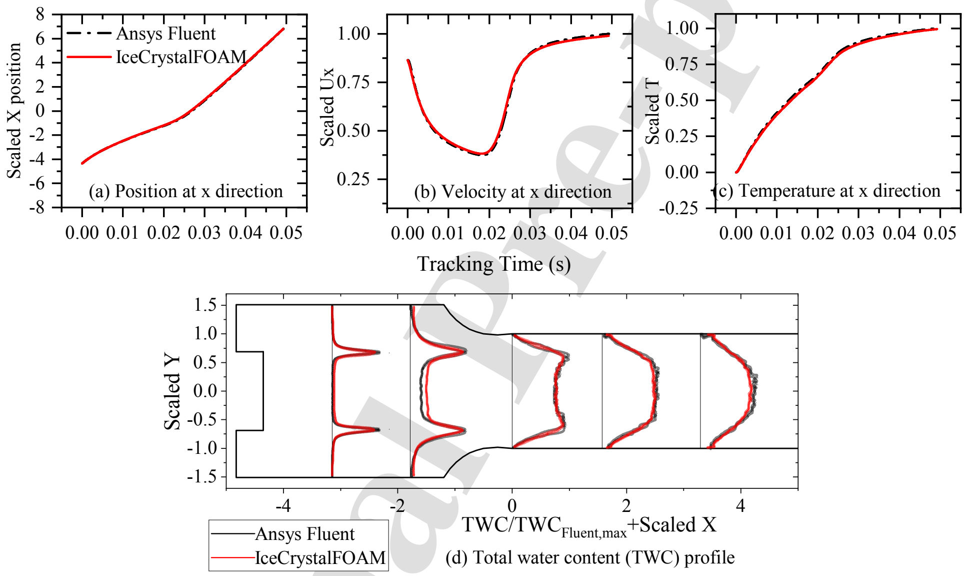

Figure 6: Comparison of the scaled particle behaviours from simulations in IceCrystalFOAM and ANSYS Fluent:(a) particle position in x direction, (b) particle velocity in x direction, (c) particle temperature, and (d) total water content.

4.1.2. Comparison against the RATFac test data

Figure 7 shows the effect of humidity on $\Delta T0$, ΔHR and the liquid water content at the measurement location [5]. As the humidity increases, both the changes in the total temperature and humidity gradually decrease, while liquid water content increases. This behavior is attributed to

[5] $\Delta T0$ and ΔHR are defined by the differences in total temperature and humidity between the dry and wet conditions, respectively.

the influence of humidity on the phase change behaviour of ice crystal particles. Higher humidity reduces the potential for vapor evaporation from the ice crystals into the continuous phase, while enhancing the heat absorbed by the particles for melting. Consequently, with the increase in the humidity, heat and mass transfer between the two phases decreases, and particle melting potential increases. The predicted changes in temperature (from 8.3 °C to 6.5 °C) and humidity (from 3.1 g/kg to 2.0 g/kg) agree well with the measurements under the same humidity conditions (from 8.0 to 6.2 °C and from 3.3 to 1.2 g/kg for total temperature and humidity, respectively). It should be noted that the observed changes in temperature and humidity are partly due to switching the operating condition from dry (without ice injection) to cold-wet (with ice injection), as indicated in Appendix B. With the increase of the humidity, the contribution of two-way coupling [6] decreases from 74% to 65% of the temperature change and from 58% to 15% of the humidity change, as shown in Fig.7(d). As $\Delta T0$ is contributed by both the particle melting and evaporation, the drop in $\Delta T0$ (9%) is much smaller than the drop in ΔHR (43%).

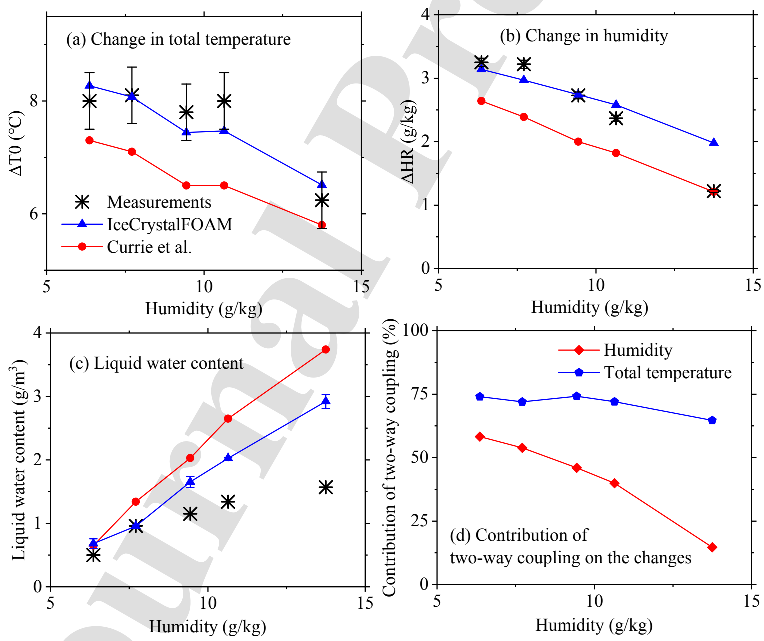

Figure 7: The effect of humidity on $\Delta T0$, ΔHR and the liquid water content at the measurement location: (a)-(c) $\Delta T0$, ΔHR and liquid water content, (d) contribution of two-way coupling on the changes.

[6] The contribution of two-way coupling is determined by $\frac{\Delta \mathrm{TH}_{\mathrm{IceOn}} - \Delta \mathrm{TH}_{\mathrm{IceOff}}}{\Delta \mathrm{TH}_{\mathrm{IceOn}}}$, where ΔTH is the change in the total temperature or humidity from the dry condition to wet condition and the subscript IceOn and IceOff represent with and without ice injection, respectively.

As shown in Fig. 7(c), although the predicted liquid water content (LWC) is qualitatively consistent with the measurements, it is overestimated, particularly at higher humidity, by about 50%–100%. Similar overprediction behavior was reported by Currie et al. [3], who observed that numerical simulations overestimated LWC by 50%–200% for the same cases investigated in this study. To date, quantitatively measuring the LWC of partially melted ice crystal particles in wind tunnels remains a challenge, as the response of SEA multiwire probes to such particles is not fully understood or calibrated, and may be affected by particle size distribution and flow velocity [8, 3, 34].

4.2. Influence of operation conditions on ice melting

Figure 8(a) [7] shows the effect of total temperature on the melt ratio (MR). The melt ratio gradually increases from the center to the wall by approximately 75% to 115% (relative difference), consistent with the temperature distribution in the working section, where the temperature rises radially outward, as shown in Fig. 5(c). In addition, MR gradually increases with the increase in the total temperature. MR increases by 115% (relative difference) at the center as the total temperature rises from 10 $°C$ to 30 $°C$. Figure 8(b) illustrates the effect of total pressure on MR. Increasing the total pressure from 34.5kPa to 74.5kPa raises the melt ratio by approximately 30%-35% (absolute difference), primarily due to the reduced evaporative cooling at higher pressure. This agrees with experimental observations indicating that, under elevated total pressure, a lower temperature is required to reproduce the same particle melting behavior [52]. Figure 8(c) presents the effect of Ma on the melt ratio. As the Ma increases from 0.2 to 0.5, MR decreases from approximately 25% to 5%. This is explained by the drop in static temperature and pressure (by approximately 11.4 K and 4.5 kPa), which weakens convective heat transfer and enhances evaporative cooling. Meanwhile, it can be observed that with increasing Ma, the MR profile gradually becomes flatter in the core and rises more steeply toward the sidewalls (increasing the scaled Y), especially at Ma = 0.5. This is due to the growth of turbulence intensity from 6.8% (Ma=0.2) to 7.7%(Ma=0.25; EXP. 7.8% [3]), 10.3%(Ma=0.4; EXP. 10.4% [3]), and 12.1%(Ma=0.5). Stronger turbulence affects transverse particle dispersion, yielding a coarser and more uniform mean diameter in the core and a sharper decrease toward the walls, as shown in Fig.8(d). This in turn produces the steeper MR rise near the walls, as shown in Fig.8(c).

[7] The parametric study is carried out based on the baseline case. The filled area around each line represents the standard deviation of the calculated melt ratio or total water content and similar filled area is also used in Fig. 9.

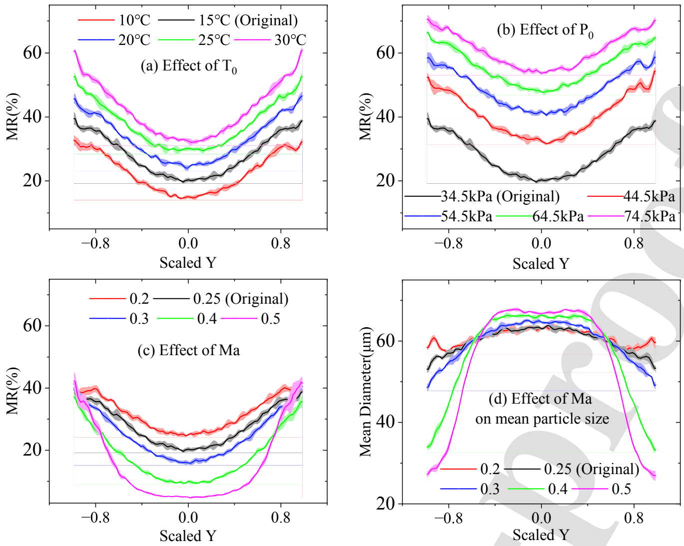

Figure 8: The effect of gas operation conditions: (a)-(c) the effects of total temperature, total pressure and Mach number on the MR, respectively; (d) the effect of Mach number on the mean particle size.

Figures 9(a)-(d) show the effect of particle size distribution (PSD) on melting behavior [8]. Figure 9(a) compares five PSDs with mean particle diameters ranging from 30 to 70 μm, showing a progressive shift of the distributions toward larger particle sizes as D_{mean} increases.The melt ratio gradually decreases with the increase in the particle size. As shown in Fig. 9(b), increasing the mean particle size from 30 μm to 52.7 μm reduces the melt ratio by approximately 0.29 (absolute mean), while a further increase from 52.7 μm to 70 μm reduces it by approximately 0.10 (absolute mean). This demonstrates an inverse but nonlinear relationship between particle size and melt ratio, as larger particles are substantially more difficult to melt than smaller ones. Figure 9(c) shows the three PSDs with the same D_{mean}. PSD2 is narrowly distributed around the intermediate particle sizes, with very limited mass fractions at both the fine and coarse ends. By contrast, PSD3 exhibits a monotonically decreasing mass fraction with increasing particle size, resulting in a substantially higher fine-particle content. Accordingly, the cumulative mass fraction of particles smaller than 20 μm is 26% for PSD3, compared with 14% for the original PSD and only 1.3% for PSD2. As shown

[8]For cases with increased mean particle size, only the minimum and maximum particle diameters are scaled according to the new mean size to modify the Rosin–Rammler PSD. For cases with the same mean particle size (D_{mean}), the spread parameter and mean diameter of the Rosin–Rammler distribution are adjusted to vary the PSD while maintaining the mean particle size.

in Fig. 9(d), with the mean size held constant, the melt ratio increases as the mass fraction of fine particles increases (PSD2 → Original PSD → PSD3). This suggests that mean particle size alone is insufficient to characterize melting potential, since the overall behavior is dictated by the full PSD. Figure 9(e) further illustrates the effect of aspect ratio, showing that increasing it from 1.5 to 20 increases the melt ratio by 0.09 (absolute mean). This indicates that nonspherical geometry enhances particle melting, because a lower sphericity increases the surface-to-mass ratio and thereby promotes heat and mass transfer, leading to greater net heat uptake per unit particle mass. Similar trends have also been reported in the literature: Hauk et al. [31] and Parker et al. [5] observed that the melting tendency of ice particles increases with increasing non-sphericity and aspect ratio, respectively. However, particle melt is more sensitive to particle size than to particle aspect ratio as reducing D_{mean} from 70 μm to 30 μm increases the melt ratio by about 2.5 times, whereas raising the aspect ratio from 1.5 to 20 increases it by only 0.3 times.

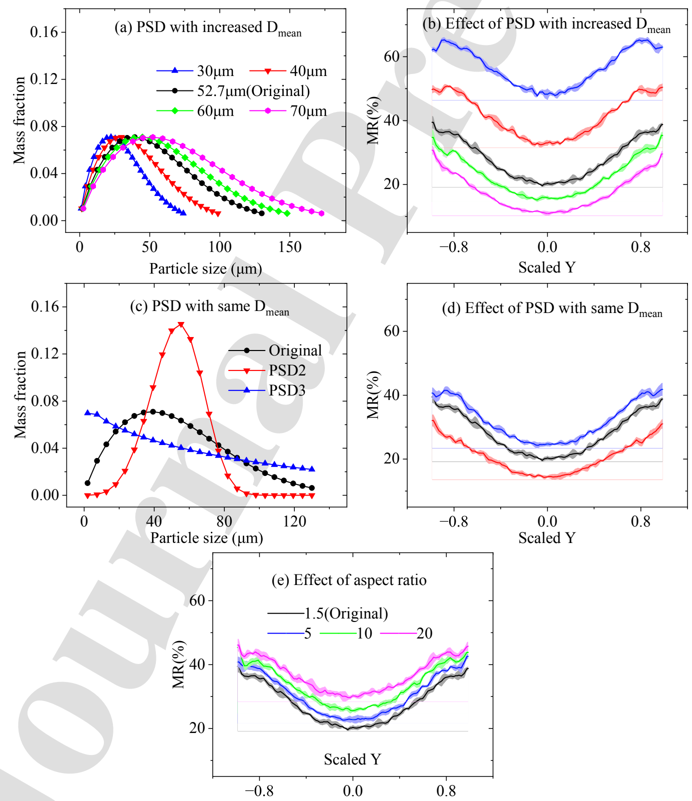

Figure 9: Effects of PSD and aspect ratio on MR: (a) five PSDs with increasing D_{mean}; (b) corresponding effects of these PSDs on MR; (c) three PSDs with the same D_{mean} but different mass-fraction distributions; (d) corresponding effects of these PSDs with the same D_{mean} on MR; (e) effect of particle aspect ratio on MR.

4.3. Remarks on modelling particle melting in the icing wind tunnel

In this study, a new two-way coupled particle-laden flow solver, IceCrystalFOAM, is developed based on the OpenFOAM framework [28], the discrete random walk model, and an ice-crystal phase-change model. The solver is used to predict the melting behavior of ice-crystal particles in the RATFac icing wind tunnel. Furthermore, by disabling the phase-change module, IceCrystal-FOAM is compared with ANSYS Fluent for code-to-code validation. The predicted flowfields and particle transport agree closely with Fluent results. The solver is also validated against experimental measurements, showing reasonably agreement in the predicted changes of total temperature and humidity, while liquid water content (LWC) matches only qualitatively, although with improved accuracy compared with the existing results by Currie et al. [3].

The performance of IceCrystalFOAM depends on the accuracy of boundary conditions for the particle phase, particularly the particle size distribution (PSD) and concentration profile. In this study, the PSD with Dv50=45μm and a 2.5 mm injection distance, following Currie et al. [3], are employed. Currie et al. [3] have noted uncertainties associated with these settings, especially when using larger PSDs and injection distances. More recently, Parker et al. [5] adopted a uniform particle concentration at the injection pipe outlet for RATFac cases, since quantitative measurements of particle concentration profiles at the boundary are lacking in both the NRC and Oxford experiments conducted in the RATFac wind tunnel. To assess these uncertainties, 25 additional numerical cases were performed using the PSD and injection location of Currie et al. [3], together with the uniform concentration distribution proposed by Parker et al. [5]. Figure 10 summarizes the predicted variations in total temperature, humidity, and LWC. Moving the injection from 2.5mm off the pipe wall to 7.5 mm, and then to a uniform inlet, slightly reduces the liquid water content, $\Delta T0$, and ΔHR. This indicates that particle melting is slightly weakened by the change in the injection. This is because the change in the initial injection position gradually places particle initially closer to the cold core region. The differences among the three injection locations, which are within approximately 0.2-0.6 $^{\circ}C$, 0.1-0.3 g/kg and 0.2-0.4 g/m^3 for temperature, humidity and liquid water content, respectively, are relatively small compared to the differences between the two PSDs. This suggests that turbulence particle dispersion alleviates the sensitivity to the initial injection location. More details on the influence of turbulence intensity on the particle behaviour can be found in Appendix C. Using coarser PSD (Dv50=57 μm, Dmean=64.6 μm) instead of the original finer PSD (Dv50=45 μm, Dmean=52.7μm) produces a stronger effect, reducing the magnitudes of $\Delta T0$, ΔHR and liquid water content by roughly 1.5-2.0 $^{\circ}C$, 0.5-1.0 g/kg, and 0.2-0.8 g/m^3, respectively. This contrast suggests that PSD (via melting rate and surface-area effects) is a more significant factor than the initial injection location in determining the thermodynamic responses. These observations further imply that careful characterization of experimental injection conditions, especially the PSD, is critical for interpreting CFD uncertainties and for calibrating LWC measurements.

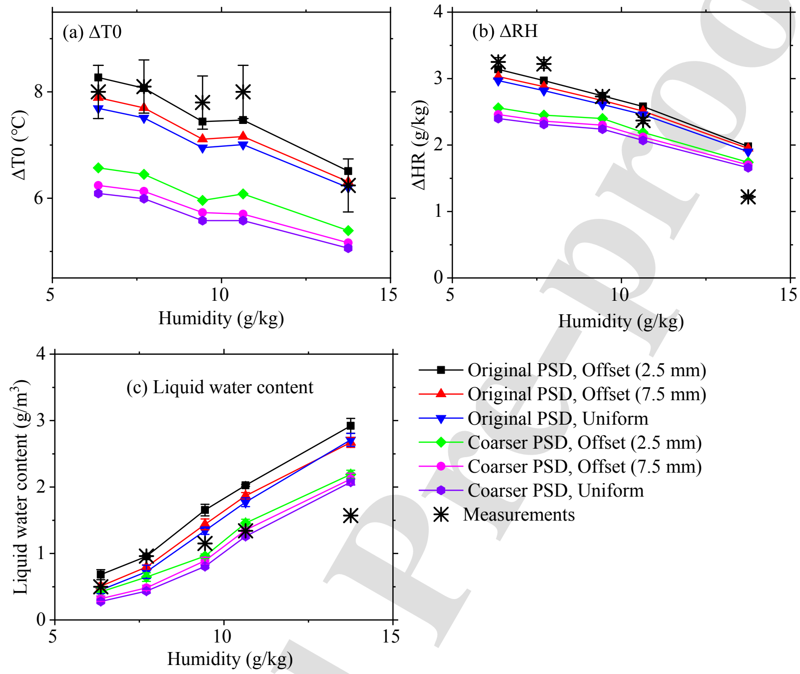

Figure 10: The effect of the particle initial locations and PSD on $\Delta T0$, ΔHR and the liquid water content at the measurement location: (a)-(c) $\Delta T0$, ΔHR and liquid water content.

5. Summary and Conclusions

A new two-way coupled Eulerian–Lagrangian solver, IceCrystalFOAM, is developed to simulate the transport and melting behavior of ice crystals in the icing wind tunnel. The solver consists of two major components: a continuous-phase module that solves the RANS equations for the fluid, and a discrete-phase module that tracks particle motion by integrating Newton's laws. A three-stage phase-change model is incorporated to predict particle melting, and a discrete random walk (DRW) model is implemented to represent turbulent dispersion. The solver's performance is assessed through comparisons with ANSYS Fluent and experimental data. The main findings are summarized as follows:

- Code-to-code validation: IceCrystalFOAM shows close agreement with ANSYS Fluent for the baseline case without melting. The predicted flowfields (velocity, turbulent kinetic energy, temperature, and humidity) and particle behavior (trajectory, velocity, temperature, and total water content) demonstrate accuracy comparable to ANSYS Fluent.
- Experimental validation and uncertainty analysis: The predicted variations in gas temperature and humidity due to two-way coupling agree well with experimental measurements, while the liquid water content (LWC) is qualitatively consistent but overestimated by approximately 50%–100%. This overprediction may stem from incomplete calibration of the measured LWC. The numerical uncertainties associated with particle injection boundary conditions—particle size distribution (PSD) and initial injection location—are also examined. Results show that PSD exerts a stronger influence on temperature, humidity, and LWC variations than injection position. This indicates that turbulent dispersion mitigates sensitivity to the injection location, whereas PSD, through its effects on melting rate and surface area, plays a dominant role in determining thermodynamic responses.
- Parametric study on melting behavior: The solver reasonably captures the influence of flow conditions and particle properties on ice melting behavior in the icing wind tunnel. Increasing humidity, total temperature, pressure, and particle aspect ratio enhances melting potential, while higher Mach numbers and larger particle sizes reduce it. Interestingly, with the mean particle size held constant, increasing the mass fraction of fine particles raises the melt ratio. This confirms that mean particle size alone is insufficient to characterize melting potential, as the overall behavior is governed by the full PSD.

Acknowledgments

This work was supported by the National Natural Science Foundation of China (Grants No. 12302327).

Appendix A. Structured mesh of the computational domain

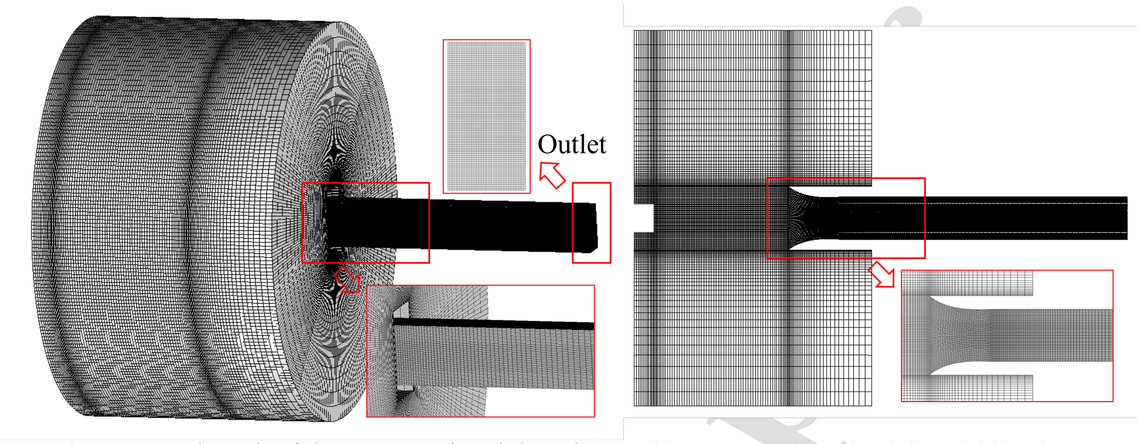

(a) Structured mesh of the computational domain (b) Structured mesh of the middle plane

Figure A.1: The structured mesh of the computational domain with orthogonal quality > 0.6 and near wall $y^+ > 60$ (mean $y^+ \approx 120$).

Appendix B. Operation conditions at the injection pipe outlet

Table B.1: Summary of operation conditions at the injection pipe outlet [3].

	Dry condition			Wet condition			
No.	$\mathrm{MFR_g}$ (kg/s)	T_0 $(°C)$	Humidity (g/kg)	$\mathrm{MFR_g}$ (kg/s)	T_0 $(°C)$	Humidity (g/kg)	$\mathrm{MFR_p}$ (kg/hr)
1	0.34	-2.8	0	0.296	-9	2.6	82.3
2	0.34	-2.8	0	0.296	-9.4	2.6	82.3
3	0.34	-2.8	0	0.296	-8.5	2.6	82.3
4	0.34	-2.8	0	0.296	-9	2.6	82.3
5	0.34	-2.8	0	0.296	-9.4	2.6	82.3

where, $\mathrm{MFR_g}$ and $\mathrm{MFR_p}$ represent the mass flow rate of gas and ice.

Appendix C. The influence of turbulence intensity on particle behaviour

To further clarify the influence of turbulence intensity on particle behaviour, 30 additional cases are performed using inlet turbulence intensities of 5% and 15%, combined with the three injection locations under five humidity conditions. It should be noted that the inlet turbulence intensity is tuned to reproduce the measured centerline turbulence intensity at the instrumentation plane. At Ma=0.25, prescribing a turbulence intensity of 10% at the injection inlet gives a predicted turbulence intensity of about 7.7% at the measurement location in the working section, which agrees well with the measured value of 7.8%.

Figure C.1 shows the predicted variations in total temperature, humidity, and LWC among the three injection locations for the inlet turbulence intensities of 5%, 10%(baseline) and 15%. It can be observed that the differences in the predicted $\Delta T0$, ΔHR, and liquid water content among the three injection locations decrease as the turbulence intensity increases. Specifically, the variations among the three injection locations decrease from 0.36–0.72 $°C$, 0.17–0.31 g/kg, and 0.29–0.41 g/m^3 to 0.22–0.41 $°C$, 0.07–0.15 g/kg, and 0.14–0.22 g/m^3, respectively, when the inlet turbulence intensity increases from 5% to 15%. These additional results further support the statement that, within the tested range, stronger turbulent dispersion reduces the sensitivity of the predicted particle behaviour to the initial injection location.

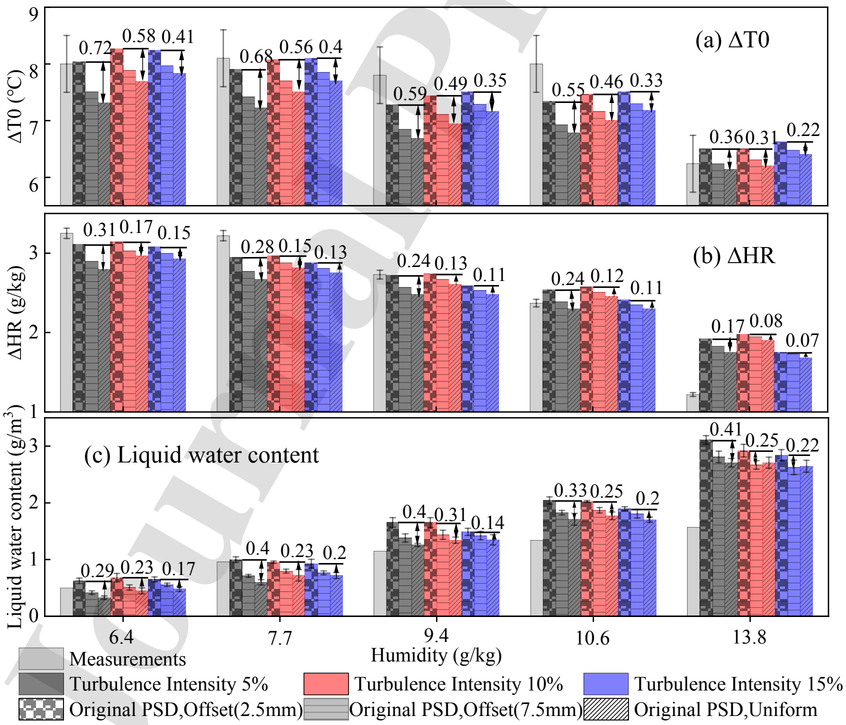

Figure C.1: The effect of inlet turbulence intensity on $\Delta T0$, ΔHR and the liquid water content at the measurement location using the original PSD: (a)-(c) $\Delta T0$, ΔHR and liquid water content.

References

[1] E. Tetteh, E. Loth, M. O. Neuteboom, J. Fisher, In-flight gas turbine engine icing: Review, AIAA Journal 60 (10) (2022) 5610–5632. doi:10.2514/1.J061523.

[2] H. Hu, L. Tian, H. Hu, Experimental investigation on ice accretion upon ice particle impacting onto heated surface, AIAA Journal 61 (7) (2023) 3019–3031. doi:10.2514/1.J062425.

[3] T. Currie, D. Fuleki, C. Davison, Simulation of ice particle melting in the NRCC RATFac mixed-phase icing tunnel, in: SAE 2015 International Conference on Icing of Aircraft, Engines, and Structures, SAE Paper 2015-01-2107, Jun. 2015. doi:10.4271/2015-01-2107.

[4] N. Zawadzki, J. Connoly, X. Yang, M. McGilvray, D. Gillespie, Ice crystal transport and accretion in a rotating test environment, in: AIAA Aviation Forum and Ascend 2024, AIAA Paper 2024-3846, 2024. doi:10.2514/6.2024-3846.

[5] L. Parker, M. McGilvray, D. R. Gillespie, G. Jones, Numerical simulations of ice particle transport at representative turbofan compressor conditions, Journal of Turbomachinery (2025) 1–14doi:10.1115/1.4068485.

[6] C. R. Davison, J. L. Chalmers, M. Neuteboom, Ice crystal environment-modular axial compressor rig: Evaluation of measured water content and melt, in: AIAA Aviation 2020 Forum, AIAA Paper 2020-2826, 2020. doi:10.2514/6.2020-2826.

[7] T. C. Currie, D. Fuleki, A. Mahallati, Experimental studies of mixed-phase sticking efficiency for ice crystal accretion in jet engines, in: 6th AIAA Atmospheric and Space Environments Conference, AIAA paper 2014-3049, 2014, p. 3049. doi:10.2514/6.2014-3049.

[8] A. Bucknell, M. McGilvray, D. R. H. Gillespie, G. Jones, A. Reed, B. Collier, Experimental studies of ice crystal accretion on axisymmetric bodies at aeroengine conditions, Journal of Propulsion and Power 36 (6) (2020) 836–850. doi:10.2514/1.B37635.

[9] B. Kott, P. M. Struk, T. P. Bartkus, A study of ice-crystal icing erosion using the NASA icing research tunnel and propulsion systems laboratory, in: AIAA Aviation 2020 Forum, AIAA paper 2020-2842, 2020, p. 2842. doi:10.2514/6.2020-2842.

[10] A. Baumert, S. Bansmer, P. Trontin, P. Villedieu, Experimental and numerical investigations on aircraft icing at mixed phase conditions, International Journal of Heat and Mass Transfer 123 (2018) 957–978. doi:10.1016/j.ijheatmasstransfer.2018.02.008.

[11] A. Bucknell, M. McGilvray, D. R. Gillespie, G. Jones, A. Reed, D. R. Buttsworth, Heat transfer in the core compressor under ice crystal icing conditions, Journal of Engineering for Gas Turbines and Power 140 (7) (2018) 071501. doi:10.1115/1.4038460.

[12] M. Neuteboom, Ice crystal environment - modular axial compressor rig: Transient analysis of ice-accretion severity, in: AIAA Aviation 2021 Forum, AIAA Paper 2021-2660, 2021. doi:10.2514/6.2021-2660.

[13] Y. A. Malik, L. Bennani, S. Bansmer, P. Trontin, P. Villedieu, Experimental and numerical investigation of accretion inception and heat transfer physics in ice crystal icing, International Journal of Heat and Mass Transfer 214 (2023) 124364. doi:10.1016/j.ijheatmasstransfer.2023.124364.

[14] T. C. Currie, Development of a small modular multi-stage axial compressor for ice crystal icing research, in: 2018 Atmospheric and Space Environments Conference, AIAA Paper 2018-4133, 2018. doi:10.2514/6.2018-4133.

[15] J. L. Chalmers, M. Neuteboom, C. R. Davison, Ice crystal environment - modular axial compressor rig: Overview of altitude icing commissioning, in: AIAA Aviation 2020 Forum, AIAA Paper 2020-2823, 2020. doi:10.2514/6.2020-2823.

[16] S. Elghobashi, On predicting particle-laden turbulent flows, Applied scientific research 52 (4) (1994) 309–329. doi:10.1007/BF00936835.

[17] J. G. Kuerten, Point-particle dns and les of particle-laden turbulent flow-a state-of-the-art review, Flow, turbulence and combustion 97 (3) (2016) 689–713. doi:10.1007/s10494-016-9765-y.

[18] M. Sommerfeld, Numerical methods for dispersed multiphase flows, in: Particles in flows, Springer, 2017, pp. 327–396. doi:10.1007/978-3-319-60282-0_6.

[19] S. Tenneti, S. Subramaniam, Particle-resolved direct numerical simulation for gas-solid flow model development, Annual Review of Fluid Mechanics 46 (Volume 46, 2014) (2014) 199–230. doi:10.1146/annurev-fluid-010313-141344.

[20] C. Marchioli, M. Bourgoin, F. Coletti, R. Fox, J. Magnaudet, M. Reeks, O. Simonin, M. Sommerfeld, F. Toschi, L.-P. Wang, S. Balachandar, Particle-laden flows, International Journal of

Multiphase Flow 191 (2025) 105291. doi:https://doi.org/10.1016/j.ijmultiphaseflow.2025.105291.

[21] C. Castang, S. Laín, D. García, M. Sommerfeld, Aerodynamic coefficients of irregular non-spherical particles at intermediate reynolds numbers, Powder Technology 402 (2022) 117341. doi:https://doi.org/10.1016/j.powtec.2022.117341.

[22] S. Subramaniam, Lagrangian–eulerian methods for multiphase flows, Progress in Energy and Combustion Science 39 (2) (2013) 215–245. doi:10.1016/j.pecs.2012.10.003.

[23] T. J. Jamaleddine, M. B. Ray, Application of computational fluid dynamics for simulation of drying processes: A review, Drying Technology 28 (2) (2010) 120–154. doi:10.1080/07373930903517458.

[24] Q. Tu, H. Wang, R. Ocone, Application of three-dimensional full-loop cfd simulation in circulating fluidized bed combustion reactors – a review, Powder Technology 399 (2022) 117181. doi:https://doi.org/10.1016/j.powtec.2022.117181.

[25] H. Yan, Z. Huang, M. Hu, J. Qi, L. Liu, Numerical modeling of gas-solid two-phase flow in a plasma melting furnace, Powder Technology 412 (2022) 117967. doi:https://doi.org/10.1016/j.powtec.2022.117967.

[26] X. Ye, C. Zhang, S. Wang, D. Yang, B. Guo, X. An, A. Yu, Simulation of desulphurization wastewater evaporation through flue gas, Powder Technology 361 (2020) 462–472. doi:https://doi.org/10.1016/j.powtec.2019.05.046.

[27] ANSYS Inc., Ansys Fluent Theory Guide (2011).

[28] Openfoam v9 (2021).
URL https://openfoam.org/version/9/

[29] T. P. Bartkus, P. Struk, J.-C. Tsao, Development of a coupled air and particle thermal model for engine icing test facilities, SAE International Journal of Aerospace 8 (2015-01-2155) (2015) 15–32. doi:10.4271/2015-01-2155.

[30] X. Yang, M. McGilvray, D. Gillespie, Numerical modeling and parametric study of the melting behavior of ice crystal particles, AIAA Journal 59 (11) (2021) 4660–4668. doi:10.2514/1.J060351.

[31] T. Hauk, E. Bonaccurso, P. Villedieu, P. Trontin, Theoretical and experimental investigation of the melting process of ice particles, Journal of Thermophysics and Heat Transfer 30 (4) (2016) 946–954. doi:10.2514/1.T4886.

[32] P. Huang, X. Bu, G. Lin, Q. Xu, C. Xiao, Simulation of coupling characteristics of motion and heat transfer between airflow and ice crystals in a single-stage compressor, Propulsion and Power Research 13 (4) (2024) 570–585. doi:10.1016/j.jppr.2024.04.003.

[33] Z. Haoran, C. Shinan, Q. Haifeng, Y. Yinglin, Numerical and experimental study on the melting of suspended ice crystals, Acta Aerodynamica Sinica (2024). doi:10.7638/kqdlxxb-2024.0102.

[34] T. Soubrié, J.-M. Senoner, P. Villedieu, M. O. Neuteboom, Ice crystal trajectory simulations in the ICE-MACR compressor rig: fragmentation and melting dynamics, in: AIAA aviation 2022 forum, AIAA Paper 2022-3535, 2022, p. 3535. doi:10.2514/6.2022-3535.

[35] J. P. Veres, P. C. Jorgenson, R. J. Coennen, Modeling of commercial turbofan engine with ice crystal ingestion; follow-on, in: 6th AIAA Atmospheric and Space Environments Conference, AIAA Paper 2014-2899, 2014, p. 2899. doi:10.2514/6.2014-2899.

[36] E. Norde, J.-M. Senoner, E. T. A. van der Weide, P. Trontin, H. W. M. Hoeijmakers, P. Villedieu, Eulerian and lagrangian ice-crystal trajectory simulations in a generic turbofan compressor, Journal of Propulsion and Power 35 (1) (2019) 26–40. doi:10.2514/1.B36916.

[37] A Coupling Model of Ice Crystal Icing in a Three-Stage Compressor, Vol. Volume 1: Aircraft Engine of Turbo Expo. doi:10.1115/GT2024-123553.

[38] W. Jia, B. Yang, Q. Kong, Numerical investigation of ice crystal melting characteristics in a multistage axial flow compressor, Applied Thermal Engineering (2025) 127081doi:10.1016/j.applthermaleng.2025.127081.

[39] P. Trontin, P. Villedieu, A comprehensive accretion model for glaciated icing conditions, International Journal of Multiphase Flow 108 (2018) 105–123. doi:10.1016/j.ijmultiphaseflow.2018.06.023.

[40] A. Bucknell, M. McGilvray, D. Gillespie, X. Yang, G. Jones, B. Collier, Icicle: A model for glaciated & mixed phase icing for application to aircraft engines, in: International Conference

on Icing of Aircraft, Engines, and Structures, SAE Paper 2019-01-1969, 2019. doi:10.4271/2019-01-1969.

[41] Y. Ma, D. Chai, X. Wang, X. Yi, Improvement of icing simulation with novel ice crystal sticking model, Journal of Aircraft 62 (3) (2025) 672–685. doi:10.2514/1.C038071.

[42] H. Qi, S. Chang, Y. Yang, P. Chang, Numerical investigations on aero-engine icing characteristics at mixed phase conditions, Applied Thermal Engineering 238 (2024) 122044. doi:10.1016/j.applthermaleng.2023.122044.

[43] W. Jones, B. Launder, The prediction of laminarization with a two-equation model of turbulence, International Journal of Heat and Mass Transfer 15 (2) (1972) 301–314. doi:10.1016/0017-9310(72)90076-2.

[44] B. Launder, D. Spalding, The numerical computation of turbulent flows, in: S. V. Patankar, A. Pollard, A. K. Singhal, S. P. Vanka (Eds.), Numerical Prediction of Flow, Heat Transfer, Turbulence and Combustion, Pergamon, 1983, pp. 96–116. doi:10.1016/B978-0-08-030937-8.50016-7.

[45] J. P. V. Doormaal, G. D. Raithby, Enhancements of the simple method for predicting incompressible fluid flows, Numerical Heat Transfer 7 (2) (1984) 147–163. doi:10.1080/01495728408961817.

[46] A. Haider, O. Levenspiel, Drag coefficient and terminal velocity of spherical and nonspherical particles, Powder Technology 58 (1) (1989) 63 – 70. doi:10.1016/0032-5910(89)80008-7.

[47] X. Yang, M. McGilvray, D. R. Gillespie, Modelling the particle trajectory and melting behaviour of non-spherical ice crystal particles, International Journal of Multiphase Flow 148 (2022) 103949. doi:10.1016/j.ijmultiphaseflow.2021.103949.

[48] A. D. Gosman, E. loannides, Aspects of computer simulation of liquid-fueled combustors, Journal of Energy 7 (6) (1983) 482–490. doi:10.2514/3.62687.

[49] D. Milojević, Lagrangian stochastic-deterministic (lsd) predictions of particle dispersion in turbulence, Particle & Particle Systems Characterization 7 (1-4) (1990) 181–190. doi:10.1002/ppsc.19900070132.

[50] P. Villedieu, P. Trontin, R. Chauvin, Glaciated and mixed phase ice accretion modeling using onera 2d icing suite, in: 6th AIAA Atmospheric and Space Environments Conference, AIAA Paper 2014-2199, 2014. doi:10.2514/6.2014-2199.

[51] M. Renksizbulut, M. C. Yuen, Experimental Study of Droplet Evaporation in a High-Temperature Air Stream, Journal of Heat Transfer 105 (2) (1983) 384–388. doi:10.1115/1.3245590.

[52] T. C. Currie, D. Fuleki, D. C. Knezevici, J. D. MacLeod, Altitude scaling of ice crystal accretion, in: 5th AIAA Atmospheric and Space Environments Conference, AIAA Paper 2013-2677, 2013, p. 2677. doi:10.2514/6.2013-2677.

[53] P. Struk, T. Currie, W. B. Wright, D. C. Knezevici, D. Fuleki, A. Broeren, M. Vargas, J.-C. Tsao, Fundamental ice crystal accretion physics studies, in: SAE 2011 International Conference on Aircraft and Engine Icing and Ground Deicing, SAE paper 2011-38-0018, 2011. doi:10.4271/2011-38-0018.

[54] X. Yang, M. McGilvray, D. Gillespie, Sticking–erosion model for ice crystal icing using particle size distribution, AIAA Journal 61 (11) (2023) 4976–4989. doi:10.2514/1.J062811.

[55] B. C. DeAngelis, E. Loth, D. Lankford, C. S. Bartlett, Simulations of turbulent droplet dispersion in wind-tunnel icing clouds, Journal of Aircraft 34 (2) (1997) 213–219. doi:10.2514/2.2159.

[56] F. Greifzu, C. Kratzsch, T. Forgber, F. Lindner, R. Schwarze, Assessment of particle-tracking models for dispersed particle-laden flows implemented in openfoam and ansys fluent, Engineering Applications of Computational Fluid Mechanics 10 (1) (2016) 30–43. doi:10.1080/19942060.2015.1104266.

Abstract:

Ice crystal icing poses a significant threat to aircraft engine safety. The sticking potential of ice crystals is mainly determined by ice melting behavior, but the coupled behavior of ice melting, turbulent dispersion, and the gas flow remains insufficiently understood. This study develops a new two-way coupled Eulerian–Lagrangian solver integrated into OpenFOAM to simulate the transport and melting behavior of ice crystals. The three-stage phase-change model is employed to capture particle melting, while turbulent dispersion is represented using the discrete random walk model. A parametric study is conducted to investigate the effects of flow conditions and particle properties on melting behavior in an icing wind tunnel. The solver is validated through code-to-code comparison and experimental data. The predicted variations in gas temperature and humidity due to two-way coupling align well with measurements, whereas the liquid water content is qualitatively consistent but overestimated. Increasing humidity, total temperature, pressure, and particle aspect ratio enhances melting potential, while higher Mach numbers and larger particle sizes reduce it. The influence of uncertainties in particle injection boundary conditions reported in the literature is also discussed.

Keywords: Particle melting; CFD; Multiphase flow; Eulerian–Lagrangian model; Ice crystal; Icing wind tunnel

Declaration of interests

☒ The authors declare that they have no known competing financial interests or personal relationships that could have appeared to influence the work reported in this paper.

☐ The authors declare the following financial interests/personal relationships which may be considered as potential competing interests: